




Article

Non-Conventional Synthesis and Repetitive Application of Magnetic Visible Light Photocatalyst Powder Consisting of Bi-Layered C-Doped TiO₂ and Ni Particles

Martynas Lelis *, Simona Tuckute , Marius Urbonavicius , Sarunas Varnagiris and Emilija Demikyte 

Center for Hydrogen Energy Technologies, Lithuanian Energy Institute, 3 Breslaujos St., 44403 Kaunas, Lithuania
* Correspondence: martynas.lelis@lei.lt; Tel.: +370-37-401-904

Abstract: In the current study, a non-conventional application of the magnetron sputtering technique was proposed. A four-step synthesis procedure allowed us to produce a magnetic photocatalyst powder consisting of bi-layered particles with carbon-doped TiO₂ on one side, and metallic Ni on the other side. XRD, SEM and EDS methods were used for sample characterization. It was determined, that after the sputtering process optimization, the bandgap of carbon-doped TiO₂ was reduced to approximately 3.1 eV and its light adsorption increased over the whole visible light spectrum. The repetitive Rhodamine B solution bleaching with magnetic photocatalyst powder and visible light showed interesting evolvement of photocatalyst efficiency. After the first cycle, Rhodamine B concentration was reduced by just 35%. However, after the second cycle, the reduction had already reached nearly 50%. Photocatalytic bleaching efficiency continued to improve rapidly until higher than 95% of Rhodamine B concentration reduction was achieved (at tenth cycle). For the next ten cycles, photocatalytic bleaching efficiency remained relatively stable. The initial gain in efficiency was attributed to the magnetic photocatalyst particle size reduction from an initial diameter of 100–150 μm to 5 μm. Naturally, the 20–30 times size reduction resulted in a remarkably increased active surface area, which was a key factor for the increased performance.



Citation: Lelis, M.; Tuckute, S.; Urbonavicius, M.; Varnagiris, S.; Demikyte, E. Non-Conventional Synthesis and Repetitive Application of Magnetic Visible Light Photocatalyst Powder Consisting of Bi-Layered C-Doped TiO₂ and Ni Particles. *Catalysts* **2023**, *13*, 169. <https://doi.org/10.3390/catal13010169>

Academic Editor: Jerry J. Wu

Received: 7 December 2022

Revised: 7 January 2023

Accepted: 9 January 2023

Published: 11 January 2023



Copyright: © 2023 by the authors. Licensee MDPI, Basel, Switzerland. This article is an open access article distributed under the terms and conditions of the Creative Commons Attribution (CC BY) license (<https://creativecommons.org/licenses/by/4.0/>).

Keywords: TiO₂; carbon doping; magnetic photocatalyst; photocatalysis; repetitive cycling; heterostructure; water treatment; Rhodamine B bleaching

1. Introduction

Titanium dioxide is a widely used commercial material with a multitude of applications. For instance, due to exceptional brightness and whiteness [1,2] TiO₂ powder is used as a white color pigment for paints, varnishes and other industrial products. But its non-toxic nature also permits to use it in human food (both as food colorant and as an additive to packaging materials), drugs, cosmetics or even implants [3–7]. In recent decades, TiO₂ also evolved as one of the key elements of emerging photocatalytic water treatment technologies.

Photocatalytic water treatment is praised for its potential to become a significant part of the new generation of waste water cleaning and disinfection technologies [8]. It utilizes semiconductive photocatalysts capability to adsorb an energy from light and to use it for the generation of electron-hole pairs. In contact with water, excited electrons and holes can create various reactive oxygen species (ROS), such as hydroxyl radicals (•OH) and superoxide anions (•O²⁻). Most of the generated ROS are strong oxidizing agents [9], whose oxidative power is even higher than the corresponding measures of traditional oxidizers, such as chlorine and ozone [10]. Hence, ROS can universally mineralize and decontaminate most of the organic and inorganic pollutants. An important advantage of photo catalytically generated ROS over traditionally used halide oxidizers is their short lifetime (for example, the lifetime of a hydroxyl radical is just a few nanoseconds [11,12]). As ROS are short-lived, just moments after irradiation termination, they relax to neutral

compounds and there is no need to take up any additional measures to remove them from the water.

Another advantage of photocatalytic water treatment is that with a proper photocatalyst the process can be initiated by natural daylight and this would be highly beneficial for the sustainable water cleaning technologies. Initially the discovery of a suitable photocatalyst was a substantial challenge, because the most suitable candidates, such as TiO_2 and ZnO , had too wide band gaps (reaching 3.2–3.37 eV [13,14]) or suffered from a fast charge recombination [15]. Eventually, after several decades of intense research, scientists provided several solutions. Elemental doping [16,17], co-catalyst loading [18], formation of heterojunctions (p-n [19,20], type-II [21,22], direct Z-scheme [23], S-scheme [24,25], Schottky junctions [26,27]), surface orientation optimization [21] and other methods [28–30] boosted the photocatalytic efficiency of photocatalysts to levels that were sufficient for practical applications. However, the attempts to adopt laboratory scale photocatalytic treatment methods to end-user products has dealt with new challenges.

One of the most pronounced obstacles was an inconvenient handling and limited reusability of photocatalyst materials [31,32]. This issue is mainly related to the nanometric or micrometric size of the most efficient photocatalyst materials, which are commonly obtained in powder form. Naturally, compression of powders into larger solid pieces, or their robust immobilization on larger substrates would solve the manageability issue. However, this would sacrifice a larger fraction of active surface area and would result in substantially reduced photocatalyst efficiency.

In the early 2000s, D. Beydoun et al. [33–35] was among the first pioneers who focused on the systematic development of magnetic photocatalysts (MP). The main idea behind the MP concept was to deposit active photocatalyst material onto fine magnetic core particles and to utilize their magnetic properties for the separation and extraction of the used photocatalyst powder. At first, the interest in MPs was not high and most of the studies were performed only with pristine TiO_2 and magnetite (or ferrites) as photocatalyst and magnetic core components, respectively [36–39]. Later, the interest in MPs grew considerably and many more photocatalyst-magnetic core pairs were investigated [40].

Analysing recently published results, it can be noticed that despite a large variety in the composition (for example some of the recent MPs studies were reported on $\text{TiO}_2/\text{ZnFe}_2\text{O}_4$ [30], $\text{TiO}_2/\text{SiO}_2/\text{Fe}_3\text{O}_4$ [41], $\text{TiO}_2/\text{SiO}_2/\text{ZnFe}_2\text{O}_4$ [42], $\text{ZnO}/\text{MnFe}_2\text{O}_4$ [43], $\text{ZrO}_2/\text{Fe}_3\text{O}_4$ [44], $\text{CoFe}_2\text{O}_4/\text{Fe}_2\text{O}_3$ [45], $\text{TiO}_2/\text{CoFe}_2\text{O}_4$ [46] etc.) generally all MPs were prepared only by wet chemical methods, namely sol-gel, co-precipitation, hydrothermal or solvothermal routes [40].

Other synthesis methods, such as physical vapor deposition (PVD) or chemical vapor deposition (CVD), are also known to produce highly active photocatalysts materials [47–49]; however, up to now their usage for the MPs synthesis was practically imperceptible. On one hand this is understandable, because potentially the most efficient form of photocatalyst materials is a powder (due to the largest specific surface area), whereas neither PVD, nor CVD are commonly applied for the powder synthesis. On the other hand, researchers have already provided evidence for all of the prerequisites which are needed for the MP synthesis by PVD or CVD methods. S. Tuckute et al. demonstrated that magnetron sputter deposition is highly capable to produce submicrometric Ni powder with considerable magnetic properties (coercivity up to 116 Oe, magnetization of powder at 10 kOe up to 43.7 emu/g) [50]. Various nanoscale nanorods, hemispherical particle arrays and other large surface area TiO_2 formations were obtained by physical methods as well [51–53]. Furthermore, magnetron sputtering and other PVD/CVD methods are well known for the quality heterostructure formation [54]. Based on the existing background, there are no clear obstacles which would not allow the use of PVD/CVD methods for the formation of bi-layered magnetic metal-photocatalytic semiconductor MP powders.

Considering earlier reports that the actual effectiveness of each particular photocatalyst material strongly depends on its synthesis method and sample history [55], we decided that it might be interesting to synthesize MP powder by an atypically applied magnetron

sputtering technique and to test its suitability for the reiterative photocatalytic treatment of contaminated water. Accordingly, in the current study magnetron sputtering based formation of MP powder was designed to produce bi-layered particles with magnetic Ni metal on one side and active carbon-doped titania photocatalyst material on the other side. Particular magnetic metal and its deposition method were selected based on the findings of our earlier study [50]. Meanwhile, carbon doped TiO_2 was chosen as a well proven photocatalyst with significant photocatalytic activity under visible light [48].

2. Results and Discussions

2.1. Formation and Characterisation of Magnetic Photocatalyst Powder

To optimize C- TiO_2 film synthesis conditions we pre-selected several pulsed-DC power rate values and used them for the deposition of undoped and carbon doped TiO_2 films. The key parameters of these experiments and hereinafter used sample nomenclature is presented at Table 1. Theoretically, if the titanium sputtering rate is low and oxygen partial pressure in deposition chamber is above the certain threshold, virtually all sputtered titanium atoms eventually should get into a contact with oxygen and should be fully oxidized. Accordingly, such coatings should be composed of perfectly stoichiometric titanium dioxide which is known to be colorless, highly transparent and has a band gap of approximately 3.25 eV [56,57]. By conducting preliminary tests, we determined that at 0.66 Pa pressure and 3.6:1 Ar: O_2 supply ratio optimal pulsed-DC magnetron power for the prototypical TiO_2 film synthesis was 280 W. The corresponding T280 sample had a mixed phase (rutile and anatase) TiO_2 crystal structure (Figure 1), its optical transmission in visible light surpassed 90% (Figure 2a) and its band gap value well fitted with the reference values [56,57] (Figure 2b). Noteworthy, in conjunction these properties essentially indicate that at lowest power rating (280 W) and fixed 0.66 Pa pressure (3.6:1 Ar: O_2 gas flow ratio) gas supply system provides enough oxygen to oxidize all titanium species (nanoclusters, atoms and ions), which are being sputtered from the unmodified Ti target.

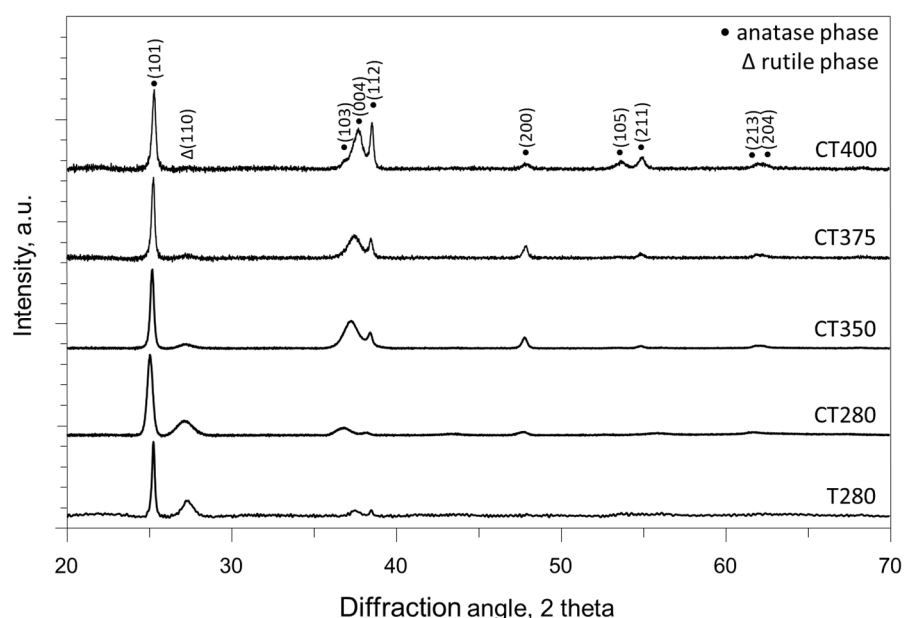
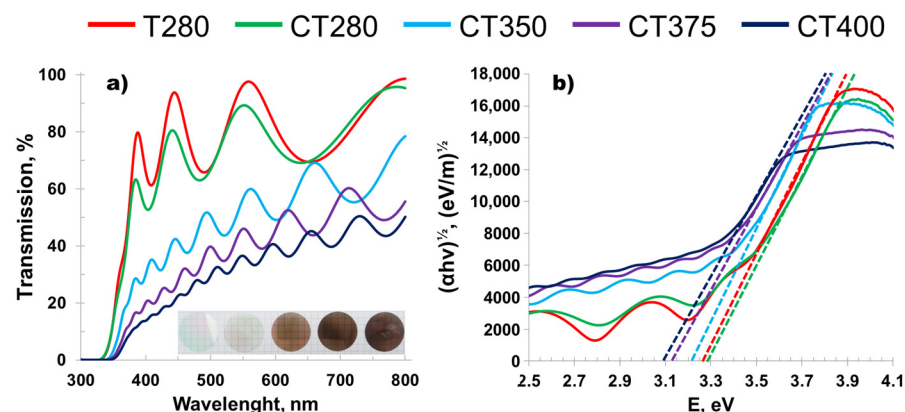


Figure 1. XRD patterns of TiO_2 and C- TiO_2 films deposited using different pulsed-DC magnetron power levels. Planes of TiO_2 anatase and TiO_2 rutile phases were indexed according to the JCPDS database cards No. 21-1272 and 21-1276, respectively.

Table 1. Key deposition parameters, optical transmission and band gap values of C-TiO₂ films.

Sample	Target	Total Gas Pressure	Ar:O ₂ Gas Supply Ratio	Pulsed-DC Power	Optical Transmission at 450 nm	Band Gap
T280	Ti	0.66 Pa	3.6:1	280 W	80%	3.26 eV
CT280	Ti with graphite insets	0.66 Pa	3.6:1	280 W	70%	3.28 eV
CT350				350 W	40%	3.22 eV
CT375				375 W	29%	3.15 eV
CT400				400 W	22%	3.10 eV

**Figure 2.** Optical properties of TiO₂ and C-TiO₂ films deposited using different pulsed-DC magnetron power levels: (a) optical transmission (inset shows natural colors of the films); and (b) Tauc plot.

When graphite insets are embedded in the Ti target, they comprehensively modify the sputtering process and affect the formation of TiO₂ based films. First, in comparison to the sputtering from the pristine Ti target, carbon insets reduce the working area of Ti metal and less of the highly reactive titanium species are sputtered from the target. Accordingly, less titanium is condensed on the surrounding surfaces (including deposition on substrate) and less oxygen is “consumed” by its chemical bonding to form titanium oxides. Altogether, even if nominal Ar:O₂ supply ratio is the same for the sputtering from pristine and modified Ti targets, carbon insets shift actual argon–oxygen balance and conditionally increase the partial pressure of oxygen.

At the same time, when sputtered carbon enters physical vapor phase, corresponding carbon species also get a chance to react with other constituents. Some of them react with oxygen to form CO and CO₂ gas molecules. Most of these molecules are directly pumped out by the constantly working vacuum pumps. However, part of them eventually hits reactive titanium species in a gas phase or gets in contact with a fresh titanium-based deposit. Considering that at low temperatures titanium affinity to oxygen is significantly higher than to carbon [58,59], the interaction between fully oxidized titanium and CO/CO₂ molecules is weak and most of the CO/CO₂ molecules are repelled away from TiO₂. The adsorption of carbonaceous molecules (and elemental carbon) by a not fully oxidized titanium is much more plausible [59] and this can lead to the formation of carbon doped TiO₂. However, even if carbon gets adsorbed at the surface, there is still a considerable probability that the growing film will be hit by oxygen, which will oxidize surface titanium and carbon constituents to TiO₂ and CO/CO₂, respectively. Naturally, in such case the later molecules are desorbed and pumped out resulting in carbon depletion from the film.

As it was explained above, using a relatively low magnetron power and Ar:O₂ supply ratio, there is enough oxygen to achieve full oxidation of the titanium, which condensates on the substrate to form the film. Accordingly, despite the relatively large surface area of the graphite insets, the above mentioned “carbon deprivation” mechanisms significantly diminish the prevalence of carbon incorporation into the growing film. Still, even at the lowest tested magnetron power a small fraction of the sputtered carbon is doped into the

augmenting film and changes in the structure and optical properties of the corresponding C-TiO₂ samples are observed. Namely, one can notice that the XRD pattern of C-TiO₂ sample deposited using 280 W pulsed DC power (sample CT280) is shifted towards lower diffraction angles (Figure 1), which can be assigned to the TiO₂ unit cell broadening by doped carbon. Similarly, there is a small reduction of optical transmission at the lower end of the visible light spectrum (Figure 2a), which is commonly attributed to the introduction of new intermediate energy levels within the TiO₂ electronic structure [60–62].

By increasing magnetron power, we intensify titanium sputtering from the target. Consequently, we indirectly alter the gas phase composition, especially close to the magnetron surface. More specifically, by sputtering additional titanium to the gas/plasma phase we increase oxygen consumption rate; therefore, we decrease oxygen partial pressure and raise the probability for titanium and carbon to reach sample surface without being fully oxidized. At the same time, higher magnetron power results in higher heat and visible UV light irradiation from the target zone. This additional activation energy helps to tilt the crystal structure formation towards a higher crystallinity anatase phase (samples CT350, CT375 and CT400), whereas the rutile phase component is gradually eliminated (Figure 1). On that account, the CT400 sample not only has more visible peaks than any other sample, it also has the sharpest anatase peaks and is the only sample without the evident presence of the rutile phase.

Figure 2 indicates that higher sputtering power reduced sample transparency from approximately 90% for CT280, to 30–40% for CT400. Similarly, the effective band gap value was also decreased from approximately 3.25–3.30 eV for samples T280/CT280 to the minimal value of 3.10 eV for sample CT400. Altogether, just by changing one parameter (i.e., magnetron power) we were able to increase the pervasion of carbon doping, alter crystal structure and modify optical properties of C-TiO₂ films.

Photocatalytic activity tests of the as deposited C-TiO₂ films under visible light (Figure 3) revealed that the most efficient sample was CT400, i.e., the film produced using the highest magnetron power. Assumingly, higher efficiency can be attributed to the uttermost carbon doping (XPS indicates approximately 2–3% of carbon inside titanium oxide) and the preferable higher crystallinity of the film [63,64]. Considering these results, we decided that C-TiO₂+Ni magnetic photocatalyst powder should be synthesized using the parameters set, which were used for the deposition of CT400 sample.

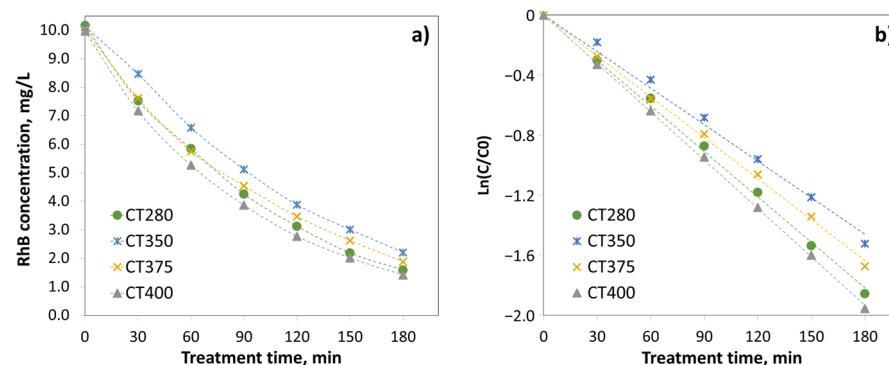


Figure 3. Photocatalytic activity of C-TiO₂ thin films under visible light irradiation: (a) RhB concentration reduction; and (b) the first-order degradation kinetics.

SEM images of the initial and coated K₂SO₄ grains are presented in Figure 4. An average size of individual grains reached up to 400–450 μm, but the grains were not continuous and smaller 100–200 μm diameter sub-grains were clearly visible in all large particles (Figure 4a,b). To obtain only the designed bi-layered film formation (the schematic view is provided in Section 3.2), during the whole deposition process the sample holder with the grains was not moved or otherwise shaken; thus, the bi-layered coating was generally formed as a glaze on a top-facing grain surface. Looking at the magnified view of the bi-layered film (Figure 4c), it can be noticed that in comparison to its thickness (approximately

1 μm) film surface contained relatively large (5–10 μm) sized features (ridges, dimples, etc.), which indicate that the curvature of the film was explicitly determined by the surface of K_2SO_4 grains. The SEM image of the washed-off magnetic photocatalyst powder (Figure 5a) revealed that they consisted of relatively wide, but thin shell-like particles. Large and small surface irregularities of the initial salt grains (Figure 4a,c) were well repeated by Ni and C-TiO₂ coatings (Figure 5b,c). The longitudinal size of C-TiO₂+Ni particles was approximately 100–150 μm and well corresponded with the average size of K_2SO_4 sub-grains revealing a characteristic film breakage along the sub-grain boundaries.

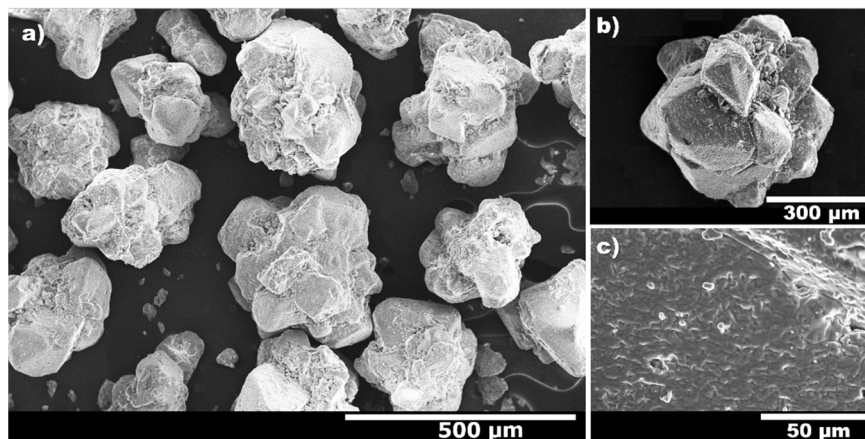


Figure 4. SEM images of K_2SO_4 grains: (a) not coated grains; (b) grains with Ni and C-TiO₂ films; and (c) magnified image of the film.

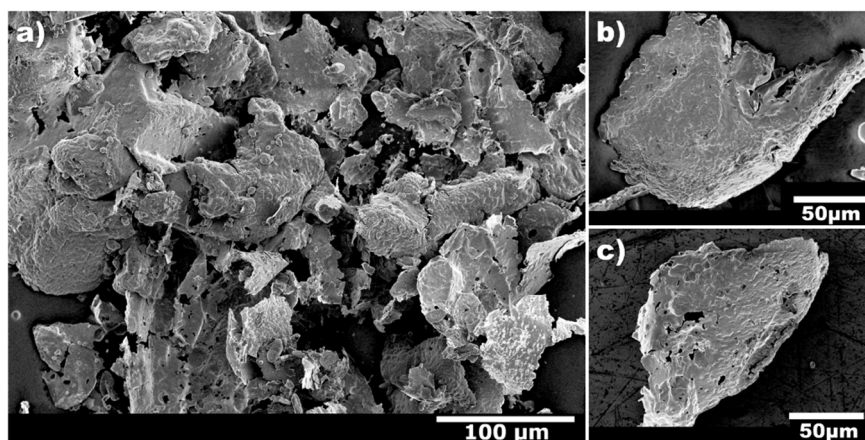


Figure 5. SEM images of the washed-off C-TiO₂+Ni particles: (a) general overview of particles; (b) the photocatalyst side of C-TiO₂+Ni particle; and (c) Ni side of C-TiO₂+Ni particle.

Elemental mapping of the washed-off particles (Figure 6) shows a clear difference between the internal and external sides of the films. The former is composed of Ni, whereas the second is dominated by Ti and O. XRD analysis of the washed-off powders (Figure 7) complements the EDS data and confirms that magnetic photocatalyst powder had metallic Ni and TiO₂ (anatase + rutile) crystal phases.

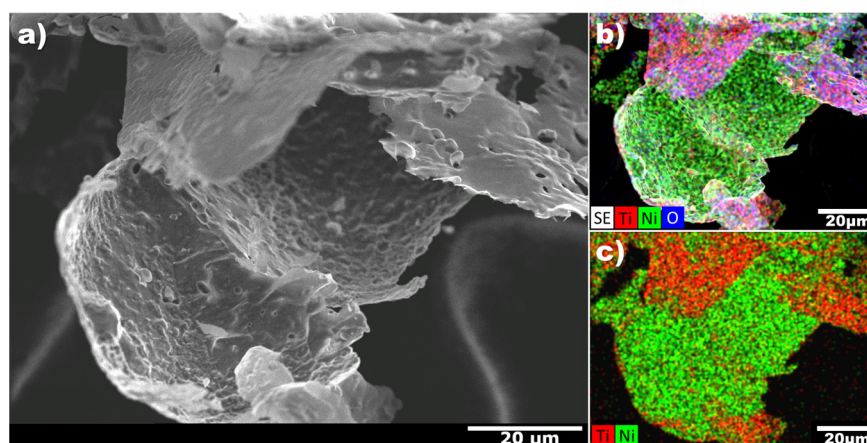


Figure 6. Elemental distribution analysis: (a) SEM image; and (b,c) EDS elemental maps of the same washed-off C-TiO₂+Ni particle. Green color in EDS mapping—nickel; red—titanium; blue—oxygen; pink—received as a “sum” of red and blue colors (in titanium oxide phase).

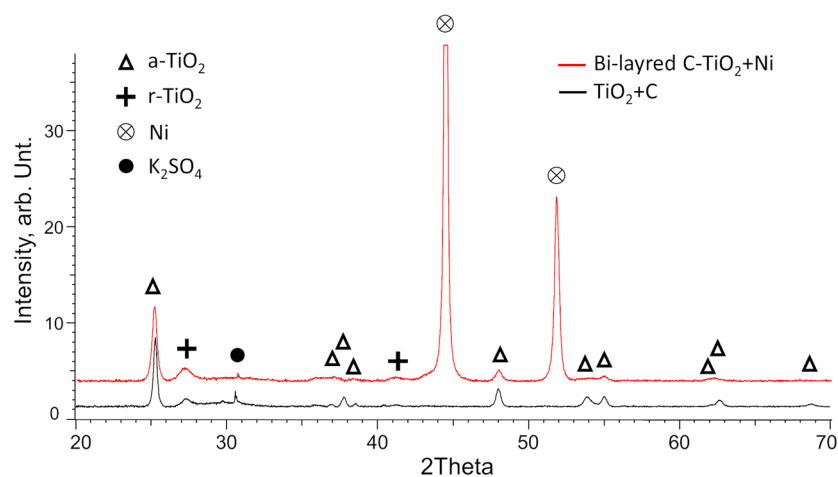


Figure 7. XRD data of the washed-off C-TiO₂ powder prepared without (black pattern) and with (red pattern) Ni underlayer. TiO₂ anatase (a-TiO₂), TiO₂ rutile (r-TiO₂), Ni and K₂SO₄ phases were indexed according to the JCPDS database cards No. 21-1272, 21-1276, 01-078-07533 and 96-120-0013, respectively.

2.2. Estimation of Photocatalytic Activity of C-TiO₂+Ni Powder

Photocatalytic efficiency and stability of C-TiO₂+Ni MP powder was assessed by performing repetitive photocatalytic bleaching of the RhB solution under visible light. Consecutive tests with the same powder set revealed an interesting evolution of its performance (Figure 8). When “fresh” C-TiO₂+Ni powder was used for the first treatment cycle, the RhB concentration was reduced by just approximately 36%. After the second cycle with the same C-TiO₂+Ni powder set, the initial RhB concentration was reduced by 45%. The trend of the rapid improvement of photocatalytic bleaching efficiency persisted for the first ten cycles. Then it stabilized at approximately 95–97% and remained generally stable for the next 7–8 cycles. Finally, during the last four cycles a small reduction in reaction efficiency was observed, though overall the RhB concentration reduction still remained higher than 90%. At the end of the last cycle all remaining MP powder were collected, rinsed with distilled water, and dried out for 48 h. The total mass of the recovered MP powder reached approximately 60% of the initial powder mass, translating into an average recovery rate of 97.5% per one cycle.

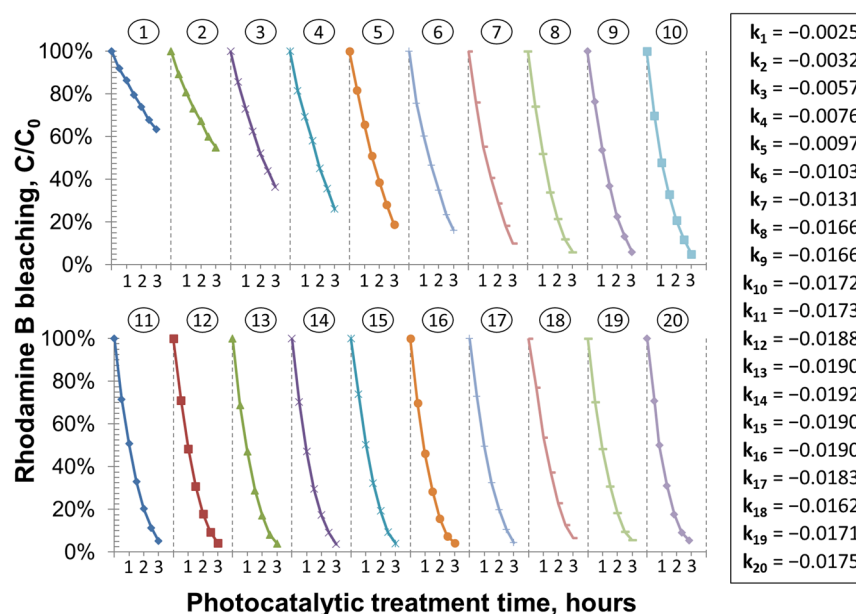


Figure 8. Evolution of C-TiO₂+Ni MP activity over 20 consecutive RhB solution bleaching cycles under visible light irradiation. Circled numbers above the curves indicate cycle order, whereas k values represent first order reaction constants (in min⁻¹ units) of the corresponding cycles.

Looking at the broader perspective, the observed photocatalytic efficiency and MP recovery rate numbers were relatively good and did not concede to the numbers reported for other mostly researched MP materials. For instance, R.A. da Silva et al. [65] conducted repetitive photocatalytic bleaching of RhB solution under visible light with MP consisting of Fe₃O₄ nanoparticles, which were coated with a photocatalytic ZnO layer. With fresh MP powder, researchers were able to achieve nearly full degradation of RhB in 8 h; however, during later cycles MP efficiency degraded significantly and was 85% and 56% after the 5th and 12th cycles, respectively. RhB bleaching by bismuth ferrites nanofibers and H₂O₂ [66] allowed up to 97.3% RhB degradation in 5 h, but just 14.3% without H₂O₂. G.Q. Tan et al. [67] reported that after 2 h treatment time bismuth ferrites, they were able to degrade 35–90% of Methyl orange with an MP recovery rate reaching 87.7–93.7% per one cycle. Despite these relative similarities in overall efficiency of MP powder, the information in Figure 8 also presents an interesting evolution at the beginning and the end of the cycling program, which were not commonly observed in other reports.

During the last five cycles first order reaction rate constant decreased from approximately -0.019 min^{-1} to -0.017 min^{-1} . Notably, an average relative decrease of rate constant ($\approx 2.2\%$ per cycle) was very similar to the average deprivation of MP powder mass ($\approx 2.5\%$ per cycle). There are numerous reports [68,69], that at moderate photocatalyst concentrations, photocatalytic bleaching rate is linearly proportional to the photocatalyst amount. Therefore, we presume that the late cycles decrease of photocatalytic bleaching efficiency is nearly entirely caused by the loss of MP material, similarly as it was concluded by [65] and other researchers.

Naturally, similar MP mass loss should be unavoidable during the first 15 treatment cycles as well. The fact that initially bleaching efficiency was increasing, demonstrates that partial MP loss was counterbalanced by an even stronger factor. To identify this factor, we re-analysed the cycled MP powder by XRD, SEM and EDS. In general, XRD and EDS elemental composition analysis did not indicate any changes between initial and cycled C-TiO₂+Ni powder. On the other hand, SEM analysis of the cycled powder revealed that magnetic stirring has reduced MP powder size tremendously, while its bi-layered structure was well preserved. Starting from the initial size of 100–150 μm the particles were broken into much smaller pieces reaching just over 5 μm in diameter (Figure 9). Such reduction of MP particle size certainly is coherent with the increase of its active surface area.

Moreover, though we did not perform any specific analysis of particle size development at intermediate stages, it is reasonable to assume that particle size was dwindling faster during the first cycles and settled down during the later ones. Altogether this implied trend and factual observance of remarkably smaller particle size well explains the observed character of MP efficiency evolution. When researchers perform MP powder synthesis by chemical methods, usually they get very fine MP powder straight away; therefore, such evolution of particle size (and efficiency) is not commonly observed.

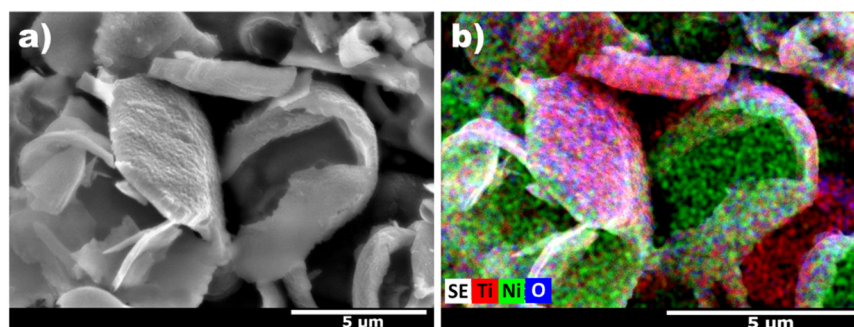


Figure 9. C-TiO₂+Ni MP powder after 20 consecutive RhB solution bleaching cycles: (a) SEM image; and (b) EDS elemental mapping.

3. Materials and Methods

3.1. Materials

K₂SO₄ salt (assay ≥ 98.0%, density 2.66 g/cm³) was obtained from Carl Roth (Karlruhe, Germany). 76 mm diameter Ni (99.99% purity) and Ti (99.99% purity) magnetron targets were obtained from Testbourne Ltd. (Bassingstoke, UK). Ar and O₂ gases (both 99.999% purity) for magnetron sputter deposition were obtained from Linde (Vilnius, Lithuania). Rhodamine B solution was prepared using distilled water and Rhodamine B powder produced by Reachem s.r.o (Bratislava, Slovakia).

3.2. Magnetic Photocatalyst Synthesis

The schematic view of the bi-layered photocatalyst powder synthesis method is presented at Figure 10. First, fine K₂SO₄ salt grains were carefully poured into low edge quartz petri-dish and uniformly spread over whole bottom of the petri-dish to avoid any visible overlapping between the grains. The grains were covered up by thin Ni layer. This ferromagnetic metal was used to provide magnetic properties for the photocatalyst particles. Then second layer consisting of active photocatalyst material, namely carbon doped titanium dioxide (C-TiO₂), was deposited on top of Ni. During the third step, coated salt grains were poured into glass vessel filled up with distilled water. In water, the salt dissolved and released solid bi-layered magnetic photocatalyst particles, which sedimented at the bottom of the vessel. Obtained MP particles were thoroughly washed off by repetitive rinsing with distilled water. After approximately ten rinsing rounds, water was fully drained off and remaining bi-layered powder were dried up for 48 h at room temperature. Ultimately, to achieve stronger crystallization of TiO₂ phase, MP powders were calcinated for 2 h at 450 °C.

Deposition of Ni and C-TiO₂ layers was conducted on K.J. Lesker PVD-75 (Jefferson Hills, PA, USA) vacuum system equipped with 76 mm diameter Torrus 3 unbalanced magnetrons. The distance between K₂SO₄ grains and Ni target was approximately 35 mm. During Ni deposition selected unbalanced magnetron was operated at a constant 300 W rate supplied by DC power source. After initial 5 min target pre-sputtering (cleaning with closed shutter), actual Ni deposition process proceeded for 3 min in inert Ar gas atmosphere (total pressure 0.6 Pa).

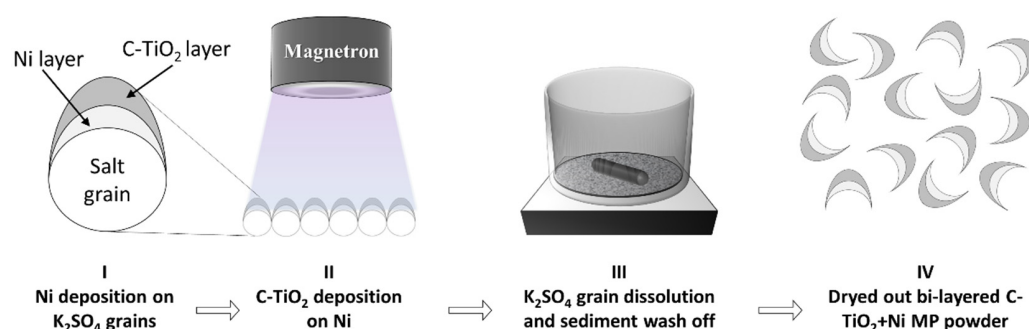


Figure 10. Schematic view of magnetic photocatalyst powder synthesis procedure.

For C-TiO₂ photocatalyst layer deposition magnetron was equipped with high purity Ti target with embedded graphite pieces (Figure 11). The ratio of exposed titanium and carbon surface areas was approximately 1:1. C-TiO₂ film deposition was performed using Ar-O₂ gas mixture at a total pressure of 0.66 Pa (Ar:O₂ gas supply ratio was approximately 3.6:1). The distance between the sample holder and Ti target was maintained at 35 mm. Typically for the most reactive metals, titanium sputtering in oxygen containing atmosphere is considerably slower and more complex process when a relatively plain deposition of Ni in inert Ar atmosphere. Accordingly, to obtain approximately 1 micrometer thick C-TiO₂ films, the deposition time was increased up to 2 h. Furthermore, to improve reactive magnetron sputtering process stability and to maintain satisfactory sputtering rate C-TiO₂ layer deposition was conducted using pulsed-DC power source [70–72].

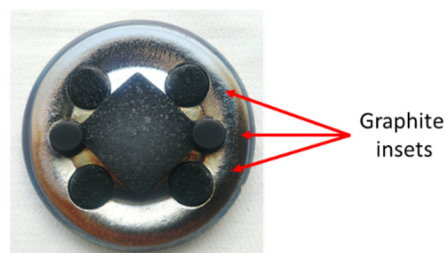


Figure 11. The image of Ti sputtering target with graphite insets.

As it is discussed in Section 2, while performing sputtering in reactive gas atmosphere, magnetron power can be a pivotal factor on the composition, structure and the prevailing phase of titanium oxide films. All these factors have a significant effect for the photocatalyst efficiency. Therefore, before synthesizing magnetic TiO₂ based photocatalyst powder we performed reactive magnetron sputtering process optimization by varying magnetron power from 280 W to 400 W. In these experiments flat 30 mm diameter borosilicate glass discs were used as the substrate for the films.

3.3. Structure Characterisation

Crystal structure of as deposited C-TiO₂ films and washed-off bi-layered C-TiO₂+Ni powder was characterized by x-ray diffraction method. The diffraction data was acquired using Bruker D8 (XRD, Bruker D8, Hamburg, Germany) instrument with Cu K α radiation working in Theta–Theta modification. Optical properties of the films were measured using UV-visible light spectrometer (Jasco V-650, Tokyo, Japan). Particle size and morphology changes were observed by Scanning Electron Microscope (SEM, Hitachi S-3400N, Tokyo, Japan). Elemental composition of the samples as well as elemental distribution maps were acquired by energy dispersive spectrometer (Bruker Quad 5040, Hamburg, Germany), which was attached to the above-mentioned SEM.

3.4. Estimation of Photocatalytic Efficiency

Photocatalytic activity of synthesized samples was tested using photocatalytic bleaching of aqueous Rhodamine B (RhB) solution. RhB dye is arguably not a perfect probe [73–75], still its usage has several advantages. On one hand, RhB remains one of toxic dyes which are still used by the industry [76], thus its degradation has a practical value. On the other hand, RhB has a relatively low visible light photolysis rate, has well described mechanism of photodegradation [77] and is successfully applied by a lot of researchers, which makes it suitable for comparisons with results from other studies. During photocatalytic treatment, RhB is degraded by two key mechanisms. First, light induced electron-hole pairs can directly interact with RhB molecules through the chemisorption mechanism to produce excited dye (Dye*) that can be converted to cationic (Dye^{•+}) and anionic (Dye^{•-}) radicals, which eventually leads to the degradation products [77]. Second, RhB can be degraded indirectly by RhB oxidation and reduction caused by reaction with O₂^{•-}, HO[•] and other reactive oxygen species which are generated by photo-excited catalyst [77].

C-TiO₂ films on flat borosilicate glass substrates were tested using RhB solution (5 mL, 10 mg/L concentration) syringed into 30 mm diameter quartz petri-dish. To prevent solution evaporation and avoid temperature fluctuations, the petri-dish was fixed onto thermostatic base (22 °C) and was covered up by thin fused silica wafer (more than 90% transmission over whole 200–2000 nm spectral range). Thorlabs SOLIS-3C (5700 K, Thorlabs, Dachau, Germany) High-Power day light white LED unit working at 90% of its nominal capacity (irradiation intensity at the solution surface approximately 230 mW/cm²) was used as a visible light source. During the experiment RhB solution was gently stirred every 15 min, and every 30 min the portion of the solution was taken out to the UV-Vis light spectrometer (Jasco V-650, Tokyo, Japan) to determine the remaining RhB concentration. After each acquisition of the transmission spectrum, whole used RhB sample volume was immediately returned back to the main petri-dish.

Proceeding to the investigation of C-TiO₂+Ni magnetic powder, the described photocatalytic activity test procedure was modified to address the evident differences between film and powder samples. First, flat bottom petri-dish was replaced by a round bottom quartz crucible (50 mm top diameter). Second, total RhB volume was increased up to 10 mL. Third, magnetic stirring bar was added to the solution. During photocatalytic treatment experiments, powder samples (initial amount was 45 mg) were stirred continuously at 700 rpm. The stirring was only temporary paused (for 2 min) before each intermediate and final specimen collection. At the periods when the stirring was switched off, magnetic photocatalyst particles rapidly reacted to the magnetic field of the stirring bar and readily agglomerated at its surface. This feature was exploited for both collecting powder-free RhB solution samples for the measurements of remaining dye concentrations, and for the change of the RhB solution between the consecutive cycles of the repetitive powder applications.

4. Conclusions

In the current study, a non-conventional application of a magnetron sputtering technique was proposed. A four-step material synthesis procedure allowed the production of magnetic photocatalyst powder consisting of bi-layered particles with carbon-doped TiO₂ on one side, and metallic Ni on the other side. After the sputtering process optimization, the band gap of carbon-doped TiO₂ was reduced to approximately 3.1 eV and its light adsorption increased over the whole visible light spectrum. Repetitive Rhodamine B solution bleaching with magnetic photocatalyst powder under visible light showed an interesting evolution in process efficiency. During the first cycle, Rhodamine B concentration was reduced by just 35%, but already during the second cycle reduction reached approximately 50%. Photocatalytic bleaching efficiency continued to improve rapidly till more than 95% of Rhodamine B was decomposed on cycle number 10. Processing through the next ten cycles, photocatalytic bleaching efficiency remained fairly stable and showed only a small deterioration during the last few cycles. The initial gain in efficiency was attributed to the magnetic photocatalyst particle size reduction by 20–30 times and a remarkably increased

active surface area. On the other hand, a small fall in efficiency at the end of the twenty-cycle testing program was attributed to the inevitable partial loss of magnetic photocatalyst, which was estimated at approximately 2.5% of the initial photocatalyst mass per one cycle.

Author Contributions: Conceptualization and methodology, M.L., S.V. and M.U.; investigation, S.T., S.V., M.U. and E.D.; writing—original draft preparation, M.L. and S.T.; writing—review and editing, M.L., S.V. and M.U.; visualization, S.T. and M.L. All authors have read and agreed to the published version of the manuscript.

Funding: This research was funded by the European Social Fund according to the activity “Improvement of researchers” qualification by implementing world-class R&D projects of measure No. 09.3.3-LMT-K-712; and project “Investigation of the application of TiO₂ and ZnO for the visible light assisted photocatalytic disinfection of biologically contaminated water” (09.3.3-LMT-K-712-01-0175).

Institutional Review Board Statement: Not applicable.

Informed Consent Statement: Not applicable.

Data Availability Statement: Not applicable.

Acknowledgments: The authors express gratitude for Giedrius Laukaitis and Kristina Bockute for their valuable input in conceptualization and interpretation of experimental results and for Mindaugas Aikas, Rolandas Uscila and Deimante Vasiliauske for their input in preparation of the samples and testing facilities.

Conflicts of Interest: The authors declare no conflict of interest.

References

1. Kischkat, J.; Peters, S.; Gruska, B.; Semstiv, M.; Chashnikova, M.; Klinkmüller, M.; Fedosenko, O.; Machulik, S.; Aleksandrova, A.; Monastyrskiy, G.; et al. Mid-infrared optical properties of thin films of aluminum oxide, titanium dioxide, silicon dioxide, aluminum nitride, and silicon nitride. *Appl. Opt.* **2012**, *51*, 6789–6798. [\[CrossRef\]](#)
2. Devore, J.R. Refractive Indices of Rutile and Sphalerite. *J. Opt. Soc. Am.* **1951**, *41*, 416–419. [\[CrossRef\]](#)
3. Titanium Dioxide, Listing of Color Additives Exempt from Certification. In *Code of Federal Regulations*; Title 21, Chapter I, Subchapter A, Part 73, Subpart A, § 73.575; Food and Drug Administration: Silver Spring, MD, USA, 2022.
4. The European Parliament and the Council of the European Union. Regulation (EC) No 1223/2009 of the European Parliament and of the Council of 30 November 2009 on cosmetic products. *Off. J. Eur. Union L* **2009**, *342*, 59–78.
5. The European Commission. Commission Directive 2008/128/EC of 22 December 2008 laying down specific purity criteria concerning colors for use in foodstuffs. *Off. J. Eur. Union* **2009**, *6*, 20–63.
6. The European Commission. Union Guidance on Regulation (EU) No 10/2011 on plastic materials and articles intended to come into contact with food as regards information in the supply chain. *Off. J. Eur. Union* **2013**, *12*, 1–32.
7. European Commission. Commission Regulation (EU) No 10/2011 of 14 January 2011 on plastic materials and articles intended to come into contact with food. *Off. J. Eur. Union* **2011**, *12*, 1–89.
8. Ren, G.; Han, H.; Wang, Y.; Liu, S.; Zhao, J.; Meng, X.; Li, Z. Recent Advances of Photocatalytic Application in Water Treatment: A Review. *Nanomaterials* **2021**, *11*, 1804. [\[CrossRef\]](#) [\[PubMed\]](#)
9. Lee, S.Y.; Park, S.J. TiO₂ photocatalyst for water treatment applications. *J. Ind. Eng. Chem.* **2013**, *19*, 1761–1769. [\[CrossRef\]](#)
10. García-Espinoza, J.D.; Robles, I.; Durán-Moreno, A.; Godínez, L.A. Photo-assisted electrochemical advanced oxidation processes for the disinfection of aqueous solutions: A review. *Chemosphere* **2021**, *274*, 129957. [\[CrossRef\]](#)
11. Sies, H. Strategies of antioxidant defense. *Eur. J. Biochem.* **1993**, *215*, 213–219. [\[CrossRef\]](#) [\[PubMed\]](#)
12. Barroso-Martínez, J.S.; BRomo, A.I.; Pudar, S.; Putnam, S.T.; Bustos, E.; Rodríguez-López, J. Real-Time Detection of Hydroxyl Radical Generated at Operating Electrodes via Redox-Active Adduct Formation Using Scanning Electrochemical Microscopy. *J. Am. Chem. Soc.* **2022**, *144*, 18896–18907. [\[CrossRef\]](#)
13. Anandan, S.; Ohashi, N.; Miyauchi, M. ZnO-based visible-light photocatalyst: Band-gap engineering and multi-electron reduction by co-catalyst. *Appl. Catal. B Environ.* **2010**, *100*, 502–509. [\[CrossRef\]](#)
14. Zhao, W.; Liu, C. Mesoporous Cu-Cu₂O@TiO₂ heterojunction photocatalysts derived from metal-organic frameworks. *RSC Adv.* **2020**, *10*, 14550–14555. [\[CrossRef\]](#)
15. Qian, R.; Zong, H.; Schneider, J.; Zhou, G.; Zhao, T.; Li, Y.; Yang, J.; Bahnemann, D.W.; Pan, J.H. Charge carrier trapping, recombination and transfer during TiO₂ photocatalysis: An overview. *Catal. Today* **2019**, *335*, 78–90. [\[CrossRef\]](#)
16. Lv, H.; Huang, Y.; Koodali, R.T.; Liu, G.; Zeng, Y.; Meng, Q.; Yuan, M. Synthesis of Sulfur-Doped 2D Graphitic Carbon Nitride Nanosheets for Efficient Photocatalytic Degradation of Phenol and Hydrogen Evolution. *ACS Appl. Mater. Interfaces* **2020**, *12*, 12656–12667. [\[CrossRef\]](#)

17. Jiang, L.; Yuan, X.; Pan, Y.; Liang, J.; Zeng, G.; Wu, Z.; Wang, H. Doping of graphitic carbon nitride for photocatalysis: A review. *Appl. Catal. B Environ.* **2017**, *217*, 388–406. [[CrossRef](#)]
18. Yan, J.; Song, Z.; Wang, X.; Xu, Y.; Pu, W.; Xu, H.; Yuan, S.; Li, H. Enhanced photocatalytic activity of ternary $\text{Ag}_3\text{PO}_4/\text{GO}/\text{g-C}_3\text{N}_4$ photocatalysts for Rhodamine B degradation under visible light radiation. *Appl. Surf. Sci.* **2019**, *466*, 70–77. [[CrossRef](#)]
19. Hunger, M.; Hüskens, G.; Brouwers, H.J.H. Photocatalytic degradation of air pollutants—From modeling to large scale application. *Cem. Concr. Res.* **2010**, *40*, 313–320. [[CrossRef](#)]
20. Tang, T.; Yin, Z.; Chen, J.; Zhang, S.; Sheng, W.; Wei, W.; Xiao, Y.; Shi, Q.; Cao, S. Novel p-n heterojunction $\text{Bi}_2\text{O}_3/\text{Ti}^{3+}\text{-TiO}_2$ photocatalyst enables the complete removal of tetracyclines under visible light. *Chem. Eng. J.* **2021**, *417*, 128058. [[CrossRef](#)]
21. Yu, J.; Low, J.; Xiao, W.; Zhou, P.; Jaroniec, M. Enhanced Photocatalytic CO_2 -Reduction Activity of Anatase TiO_2 by Coexposed {001} and {101} Facets. *J. Am. Chem. Soc.* **2014**, *136*, 8839–8842. [[CrossRef](#)]
22. Ong, W.-J.; Tan, L.-L.; Chai, S.-P.; Yong, S.-T.; Mohamed, A.R. Highly reactive {001} facets of TiO_2 -based composites: Synthesis, formation mechanism and characterization. *Nanoscale* **2014**, *6*, 1946–2008. [[CrossRef](#)]
23. Xu, Q.; Zhang, L.; Yu, J.; Wageh, S.; Al-Ghamdi, A.A.; Jaroniec, M. Direct Z-scheme photocatalysts: Principles, synthesis, and applications. *Mater. Today* **2018**, *21*, 1042–1063. [[CrossRef](#)]
24. Wang, J.; Wang, G.; Cheng, B.; Yu, J.; Fan, J. Sulfur-doped $\text{g-C}_3\text{N}_4/\text{TiO}_2$ S-scheme heterojunction photocatalyst for Congo Red photodegradation. *Chin. J. Catal.* **2021**, *42*, 56–68. [[CrossRef](#)]
25. Fu, J.; Xu, Q.; Low, J.; Jiang, C.; Yu, J. Ultrathin 2D/ $2\text{D WO}_3/\text{g-C}_3\text{N}_4$ step-scheme H_2 -production photocatalyst. *Appl. Catal. B Environ.* **2019**, *243*, 556–565. [[CrossRef](#)]
26. Feng, X.; Yu, Z.; Sun, Y.; Shan, M.; Long, R.; Li, X. 3D MXene/ Ag_2S material as Schottky junction catalyst with stable and enhanced photocatalytic activity and photocorrosion resistance. *Sep. Purif. Technol.* **2021**, *266*, 118606. [[CrossRef](#)]
27. Li, W.; Chu, X.; He, S.; Wang, X.; Wang, C. A gourd-like hollow mesoporous silica particle-supported Ag/AgBr Schottky junction for highly efficient mineralization of tetracycline hydrochloride. *Environ. Sci. Nano* **2020**, *7*, 2654–2668. [[CrossRef](#)]
28. Thongam, D.D.; Chaturvedi, H. Advances in nanomaterials for heterogeneous photocatalysis. *Nano Express* **2021**, *2*, 12005. [[CrossRef](#)]
29. Védrine, J.C. Importance, features and uses of metal oxide catalysts in heterogeneous catalysis. *Chin. J. Catal.* **2019**, *40*, 1627–1636. [[CrossRef](#)]
30. Chen, R.; Ding, S.; Wang, B.; Ren, X. Preparation of $\text{ZnFe}_2\text{O}_4/\text{TiO}_2$ Novel Core-Shell Photocatalyst by Ultrasonic Method and Its Photocatalytic Degradation Activity. *Coatings* **2022**, *12*, 1407. [[CrossRef](#)]
31. Shan, A.Y.; Ghazi, T.I.M.; Rashid, S.A. Immobilisation of titanium dioxide onto supporting materials in heterogeneous photocatalysis: A review. *Appl. Catal. A Gen.* **2010**, *389*, 1–8. [[CrossRef](#)]
32. Srikanth, B.; Goutham, R.; Badri Narayan, R.; Ramprasath, A.; Gopinath, K.P.; Sankaranarayanan, A.R. Recent advancements in supporting materials for immobilised photocatalytic applications in waste water treatment. *J. Environ. Manag.* **2017**, *200*, 60–78. [[CrossRef](#)]
33. Beydoun, D.; Amal, R.; Low, G.K.-C.; McEvoy, S. Novel Photocatalyst: Titania-Coated Magnetite. Activity and Photodissolution. *J. Phys. Chem. B* **2000**, *104*, 4387–4396. [[CrossRef](#)]
34. Beydoun, D.; Amal, R. Implications of heat treatment on the properties of a magnetic iron oxide–titanium dioxide photocatalyst. *Mater. Sci. Eng. B* **2002**, *94*, 71–81. [[CrossRef](#)]
35. Watson, S.; Beydoun, D.; Amal, R. Synthesis of a novel magnetic photocatalyst by direct deposition of nanosized TiO_2 crystals onto a magnetic core. *J. Photochem. Photobiol. A Chem.* **2002**, *148*, 303–313. [[CrossRef](#)]
36. Fu, W.; Yang, H.; Li, M.; Li, M.; Yang, N.; Zou, G. Anatase TiO_2 nanolayer coating on cobalt ferrite nanoparticles for magnetic photocatalyst. *Mater. Lett.* **2005**, *59*, 3530–3534. [[CrossRef](#)]
37. Xu, M.-W.; Bao, S.-J.; Zhang, X.-G. Enhanced photocatalytic activity of magnetic TiO_2 photocatalyst by silver deposition. *Mater. Lett.* **2005**, *59*, 2194–2198. [[CrossRef](#)]
38. Xu, S.; Shangguan, W.; Yuan, J.; Chen, M.; Shi, J. Preparations and photocatalytic properties of magnetically separable nitrogen-doped TiO_2 supported on nickel ferrite. *Appl. Catal. B Environ.* **2007**, *71*, 177–184. [[CrossRef](#)]
39. Ao, Y.; Xu, J.; Zhang, S.; Fu, D. Synthesis of a magnetically separable composite photocatalyst with high photocatalytic activity under sunlight. *J. Phys. Chem. Solids* **2009**, *70*, 1042–1047. [[CrossRef](#)]
40. Jacinto, M.J.; Ferreira, L.F.; Silva, V.C. Magnetic materials for photocatalytic applications—A review. *J. Sol-Gel Sci. Technol.* **2020**, *96*, 1–14. [[CrossRef](#)]
41. Chen, Z.-Y.; Lai, W.W.-P.; Lin, H.H.-H.; Tan, J.X.; Wu, K.C.-W.; Lin, A.Y.-C. Photocatalytic degradation of ketamine using a reusable $\text{TiO}_2/\text{SiO}_2/\text{Fe}_3\text{O}_4$ magnetic photocatalyst under simulated solar light. *J. Environ. Chem. Eng.* **2022**, *10*, 108637. [[CrossRef](#)]
42. Mrotek, E.; Dudziak, S.; Malinowska, I.; Pelczarski, D.; Rzyńska, Z.; Zielińska-Jurek, A. Improved degradation of etodolac in the presence of core-shell $\text{ZnFe}_2\text{O}_4/\text{SiO}_2/\text{TiO}_2$ magnetic photocatalyst. *Sci. Total Environ.* **2020**, *724*, 138167. [[CrossRef](#)]
43. Duarte, F.D.; Melo, A.L.; Ferro, A.D.; Zanta, C.L.; Duarte, J.L.; Oliveira, R.M. Magnetic Zinc Oxide/Manganese Ferrite Composite for Photodegradation of the Antibiotic Rifampicin. *Materials* **2022**, *15*, 8185. [[CrossRef](#)] [[PubMed](#)]
44. Banić, N.; Šojić Merkulov, D.; Despotović, V.; Finčur, N.; Ivetić, T.; Bognár, S.; Jovanović, D.; Abramović, B. Rapid Removal of Organic Pollutants from Aqueous Systems under Solar Irradiation Using $\text{ZrO}_2/\text{Fe}_3\text{O}_4$ Nanoparticles. *Molecules* **2022**, *27*, 8060. [[CrossRef](#)] [[PubMed](#)]

45. Soares, J.D.; Cavalcanti, W.E.; Torres, M.A.; Pergher, S.B.; De Oliveira, F.J.; Braga, T.P. Synthesis, Characterization and Photocatalytic Activity of $\text{CoFe}_2\text{O}_4/\text{Fe}_2\text{O}_3$ Dispersed in Mesoporous KIT-6. *Nanomaterials* **2022**, *12*, 3566. [[CrossRef](#)]
46. Ibrahim, I.; Belessiotis, G.V.; Elseman, A.M.; Mohamed, M.M.; Ren, Y.; Salama, T.M.; Mohamed, M.B.I. Magnetic $\text{TiO}_2/\text{CoFe}_2\text{O}_4$ Photocatalysts for Degradation of Organic Dyes and Pharmaceuticals without Oxidants. *Nanomaterials* **2022**, *12*, 3290. [[CrossRef](#)]
47. Görgün, N.; Özer, Ç.; Polat, K. A new catalyst material from electrospun PVDF-HFP nanofibers by using magnetron-sputter coating for the treatment of dye-polluted waters. *Adv. Compos. Hybrid Mater.* **2019**, *2*, 423–430. [[CrossRef](#)]
48. Varnagir, S.; Medvids, A.; Lelis, M.; Milcius, D.; Antuzevics, A. Black carbon-doped TiO_2 films: Synthesis, characterization and photocatalysis. *J. Photochem. Photobiol. A Chem.* **2019**, *382*, 111941. [[CrossRef](#)]
49. Zhang, L.; Guo, J.; Hao, B.; Ma, H. WO_3/TiO_2 heterojunction photocatalyst prepared by reactive magnetron sputtering for Rhodamine B dye degradation. *Opt. Mater.* **2022**, *133*, 113035. [[CrossRef](#)]
50. Tučkutė, S.; Urbonavičius, M.; Lelis, M.; Maiorov, M.; Ordaz, J.R.D.; Milčius, D. A new method of nanocrystalline nickel powder formation by magnetron sputtering on the water-soluble substrates. *Mater. Res. Express* **2018**, *5*, 015017. [[CrossRef](#)]
51. Li, Y.; Sasaki, T.; Shimizu, Y.; Koshizaki, N. Hexagonal-Close-Packed, Hierarchical Amorphous TiO_2 Nanocolumn Arrays: Transferability, Enhanced Photocatalytic Activity, and Superamphiphilicity without UV Irradiation. *J. Am. Chem. Soc.* **2008**, *130*, 14755–14762. [[CrossRef](#)]
52. Li, B.Y.; Fang, X.; Koshizaki, N.; Sasaki, T.; Li, L.; Gao, S.; Shimizu, Y.; Bando, Y.; Golberg, D. Periodic TiO_2 Nanorod Arrays with Hexagonal Nonclose-Packed Arrangements: Excellent Field Emitters by Parameter Optimization. *Adv. Funct. Mater.* **2009**, *19*, 2467–2473. [[CrossRef](#)]
53. Li, Y.; Sasaki, T.; Shimizu, Y.; Koshizaki, N. A Hierarchically Ordered TiO_2 Hemispherical Particle Array with Hexagonal-Non-Close-Packed Tops: Synthesis and Stable Superhydrophilicity without UV Irradiation. *Small* **2008**, *4*, 2286–2291. [[CrossRef](#)] [[PubMed](#)]
54. Hui, W.; Guodong, S.; Xiaoshu, Z.; Wei, Z.; Lin, H.; Ying, Y. In-situ synthesis of TiO_2 rutile/anatase heterostructure by DC magnetron sputtering at room temperature and thickness effect of outermost rutile layer on photocatalysis. *J. Environ. Sci.* **2017**, *60*, 33–42. [[CrossRef](#)] [[PubMed](#)]
55. Ellmer, K. Magnetron sputtering of transparent conductive zinc oxide: Relation between the sputtering parameters and the electronic properties. *J. Phys. D Appl. Phys.* **2000**, *33*, R17–R32. [[CrossRef](#)]
56. Khan, M.M.; Ansari, S.A.; Pradhan, D.; Ansari, M.O.; Han, D.H.; Lee, J.; Cho, M.H. Band gap engineered TiO_2 nanoparticles for visible light induced photoelectrochemical and photocatalytic studies. *J. Mater. Chem. A* **2014**, *2*, 637–644. [[CrossRef](#)]
57. Židek, K.; Hlubuček, J.; Horodyská, P.; Budasz, J.; Václavík, J. Analysis of sub-bandgap losses in TiO_2 coating deposited via single and dual ion beam deposition. *Thin Solid Film.* **2017**, *626*, 60–65. [[CrossRef](#)]
58. Arvieu, C.; Manaud, J.P.; Quenisset, J.M. Interaction between titanium and carbon at moderate temperatures. *J. Alloys Compd.* **2004**, *368*, 116–122. [[CrossRef](#)]
59. Dodson, L.G.; Thompson, M.C.; Weber, J.M. Titanium Insertion into CO Bonds in Anionic Ti–CO₂ Complexes. *J. Phys. Chem. A* **2018**, *122*, 2983–2991. [[CrossRef](#)]
60. Zhao, L.; Chen, X.; Wang, X.; Zhang, Y.; Wei, W.; Sun, Y.; Antonietti, M.; Titirici, M.-M. One-Step Solvothermal Synthesis of a Carbon@ TiO_2 Dyade Structure Effectively Promoting Visible-Light Photocatalysis. *Adv. Mater.* **2010**, *22*, 3317–3321. [[CrossRef](#)]
61. Wang, X.; Meng, S.; Zhang, X.; Wang, H.; Zhong, W.; Du, Q. Multi-type carbon doping of TiO_2 photocatalyst. *Chem. Phys. Lett.* **2007**, *444*, 292–296. [[CrossRef](#)]
62. Noorimotlagh, Z.; Kazeminezhad, I.; Jaafarzadeh, N.; Ahmadi, M.; Ramezani, Z.; Silva Martinez, S. The visible-light photodegradation of nonylphenol in the presence of carbon-doped TiO_2 with rutile/anatase ratio coated on GAC: Effect of parameters and degradation mechanism. *J. Hazard. Mater.* **2018**, *350*, 108–120. [[CrossRef](#)]
63. Wu, H.; Ma, J.; Zhang, C.; He, H. Effect of TiO_2 calcination temperature on the photocatalytic oxidation of gaseous NH_3 . *J. Environ. Sci.* **2014**, *26*, 673–682. [[CrossRef](#)] [[PubMed](#)]
64. Sienkiewicz, A.; Wanag, A.; Kusiak-Nejman, E.; Ekiert, E.; Rokicka-Konieczna, P.; Morawski, A.W. Effect of calcination on the photocatalytic activity and stability of TiO_2 photocatalysts modified with APTES. *J. Environ. Chem. Eng.* **2021**, *9*, 104794. [[CrossRef](#)]
65. da Silva, R.A.; Jacinto, M.J.; Silva, V.C.; Cabana, D.C. Urea-assisted fabrication of $\text{Fe}_3\text{O}_4@\text{ZnO}@\text{Au}$ composites for the catalytic photodegradation of Rhodamine-B. *J. Sol-Gel Sci. Technol.* **2018**, *86*, 94–103. [[CrossRef](#)]
66. Wang, W.; Li, N.; Chi, Y.; Li, Y.; Yan, W.; Li, X.; Shao, C. Electrospinning of magnetical bismuth ferrite nanofibers with photocatalytic activity. *Ceram. Int.* **2013**, *39*, 3511–3518. [[CrossRef](#)]
67. Tan, G.-Q.; Zheng, Y.-Q.; Miao, H.-Y.; Xia, A.; Ren, H.-J. Controllable Microwave Hydrothermal Synthesis of Bismuth Ferrites and Photocatalytic Characterization. *J. Am. Ceram. Soc.* **2012**, *95*, 280–289. [[CrossRef](#)]
68. Khan, I.; Saeed, K.; Zekker, I.; Zhang, B.; Hendi, A.H.; Ahmad, A.; Ahmad, S.; Zada, N.; Ahmad, H.; Shah, L.A.; et al. Review on Methylene Blue: Its Properties, Uses, Toxicity and Photodegradation. *Water* **2022**, *14*, 242. [[CrossRef](#)]
69. Zhu, X.; Castleberry, S.R.; Nanny, M.A.; Butler, E.C. Effects of pH and Catalyst Concentration on Photocatalytic Oxidation of Aqueous Ammonia and Nitrite in Titanium Dioxide Suspensions. *Environ. Sci. Technol.* **2005**, *39*, 3784–3791. [[CrossRef](#)]
70. Yeh, T.-S.; Wu, J.-M.; Hu, L.-J. The properties of TiN thin films deposited by pulsed direct current magnetron sputtering. *Thin Solid Film.* **2008**, *516*, 7294–7298. [[CrossRef](#)]

71. Cooke, K.E.; Hampshire, J.; Southall, W.; Teer, D.G. Industrial Application of Pulsed Dc Bias Power Supplies in Closed Field Unbalanced Magnetron Sputter Ion Plating. *Surf. Eng.* **2004**, *20*, 189–195. [[CrossRef](#)]
72. Vlček, J.; Pajdarová, A.D.; Musil, J. Pulsed dc Magnetron Discharges and their Utilization in Plasma Surface Engineering. *Contrib. Plasma Phys.* **2004**, *44*, 426–436. [[CrossRef](#)]
73. Sun, H.; Guo, F.; Pan, J.; Huang, W.; Wang, K.; Shi, W. One-pot thermal polymerization route to prepare N-deficient modified g-C₃N₄ for the degradation of tetracycline by the synergistic effect of photocatalysis and persulfate-based advanced oxidation process. *Chem. Eng. J.* **2021**, *406*, 126844. [[CrossRef](#)]
74. Liu, X.; Gu, S.; Zhao, Y.; Zhou, G.; Li, W. BiVO₄, Bi₂WO₆ and Bi₂MoO₆ photocatalysis: A brief review. *J. Mater. Sci. Technol.* **2020**, *56*, 45–68. [[CrossRef](#)]
75. Li, H.; Li, W.; Liu, X.; Ren, C.; Miao, X.; Li, X. Engineering of Gd/Er/Lu-triple-doped Bi₂MoO₆ to synergistically boost the photocatalytic performance in three different aspects: Oxidizability, light absorption and charge separation. *Appl. Surf. Sci.* **2019**, *463*, 556–565. [[CrossRef](#)]
76. Zada, N.; Saeed, K.; Khan, I. Decolorization of Rhodamine B dye by using multiwalled carbon nanotubes/Co–Ti oxides nanocomposite and Co–Ti oxides as photocatalysts. *Appl. Water Sci.* **2019**, *10*, 40. [[CrossRef](#)]
77. Khan, I.; Saeed, K.; Ali, N.; Khan, I.; Zhang, B.; Sadiq, M. Heterogeneous photodegradation of industrial dyes: An insight to different mechanisms and rate affecting parameters. *J. Environ. Chem. Eng.* **2020**, *8*, 104364. [[CrossRef](#)]

Disclaimer/Publisher’s Note: The statements, opinions and data contained in all publications are solely those of the individual author(s) and contributor(s) and not of MDPI and/or the editor(s). MDPI and/or the editor(s) disclaim responsibility for any injury to people or property resulting from any ideas, methods, instructions or products referred to in the content.